Comparison of Experimental and Numerical Results for Delta Wings with Vortex Flaps

Kenneth G. Powell* and Earll M. Murman†
Massachusetts Institute of Technology, Cambridge, Massachusetts
and
Richard M. Wood‡ and David S. Miller‡
NASA Langley Research Center, Hampton, Virginia

Computational and experimental results are presented for delta wings with vortex flaps. The wings have an undeflected leading-edge sweep of 75 deg. Flap angles of 5 and 10 deg, measured in the streamwise direction, are considered. The nominal angle of attack is varied from 4 to 12 deg. Results for freestream Mach numbers of 1.7 and 2.4 are shown. Surface pressures and vapor screens are given for the experimental data. Surface pressures, crossflow velocities, total pressure loss, and crossflow Mach number are given for the numerical data. C_l vs α curves are shown for experimental and computational results. The Euler equation model correctly predicts the topology of the flow in each of the cases considered. The lift is predicted well at the higher angles of attack, but is slightly overpredicted at the lower angles of attack.

Introduction

COMPRESSIBLE flow past sharp-edged delta wings can lead to a variety of flow patterns. Stanbrook and Squire[1] originally postulated the classification of these flows as a function of angle of attack normal to the leading edge and Mach number normal to the leading edge. This classification has been extended by Miller and Wood[2] to include the different flow topologies seen in their experiments. In addition, Vorropoulos and Wendt[3] added a regime for leading-edge vortices with crossflow shocks under them.

Interest in these flows has spread to the world of computational fluid dynamics, with the result that a number of computational studies employing the Euler equations[4-8] and the Reynolds-averaged Navier-Stokes equations[7-11] have been reported. Most of the experimentally observed flow regimes have been reproduced in the various calculations.

The present study uses the conical Euler equations to model the flow. The advantage of using the Euler equations as opposed to the Reynolds-averaged Navier-Stokes equations is that they are less expensive to solve. The disadvantage is that they do not model viscous effects, such as the boundary layer on the wing, and the secondary separation under the primary vortex. The conical self-similarity assumption further simplifies the problem by reducing the number of dimensions.

The justification of the use of the Euler equations is based on the fact that the geometry being modeled is sharp-edged. Because of this, there is a Kutta condition fixing the separation point at the leading edge, independent of the Reynolds number. Therefore, any computational model that has a diffusive effect at the leading edge that mimics real diffusive effects should trigger separation, regardless of the magnitude of the diffusion. The discretized Euler equations are diffusive near the leading edge, due to truncation error and added artificial viscosity. The Kutta condition will therefore be enforced, and the discretized Euler equations should be expected to model the separation and primary vortex very well. Experience shows this to be the case.[6,12]

The justification of the use of the conical self-similarity assumption is based on the fact that the model used in the experiment is approximately conical and the freestream is supersonic. The Euler equations permit a conical solution if the boundary conditions are conical, i.e., if the bow shock and the body can be generated by rays through the apex of the wing. Subsonic flow is not strictly conical. For the model used in the experiment, the upper surface of the wing and the flap are conical; the centerbody and the lower surface are not (see Fig. 1). Although experimental pressure distributions at different stations along the length of the configuration are not shown in this paper, they are essentially conical.

Flows with either leading-edge vortices or leading-edge separation bubbles are characterized by low-pressure regions on the leeward side of the wing. A pressure distribution of this type is desirable in that it gives high lift. On a flat wing,

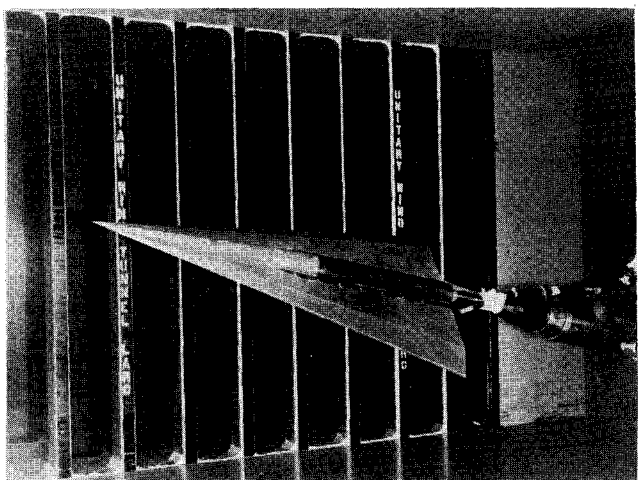
CONICAL WING-FLAP MODEL

Fig. 1 Experimental model.

Presented as Paper 86-1840 at the AIAA 4th Applied Aerodynamics Conference, San Diego, CA, June 9-11, 1986; received Aug. 19, 1986; revision received July 31, 1987.

*Research Assistant, Computational Fluid Dynamics Laboratory, Department of Aeronautics and Astronautics; currently Assistant Professor, Department of Aerospace Engineering, The University of Michigan. Member AIAA.

†Professor, Computational Fluid Dynamics Laboratory, Department of Aeronautics and Astronautics. Fellow AIAA.

‡Research Scientist, Fundamental Aerodynamics Branch. Member AIAA.

however, a pressure distribution of this type also implies high drag. If it were possible to camber the wing so that the low-pressure region resided over a portion of the wing with a forward-facing normal, this would result in both lift and thrust. This is the basic idea behind vortex flaps. The first experimental demonstration of the drag-reduction potential of vortex flaps took place at NASA Langley Research Center[13] and there has been a sizable effort in vortex-flap research there since then.[14] Some preliminary computational results have been presented by Arlinger[4] and Murman et al.,[6] but this paper is the first extensive comparison of Euler solutions and experimental data for vortex-flap geometries.

Governing Equations

The three-dimensional unsteady Euler equations in conservation form are

$$\frac{\partial}{\partial t}\begin{bmatrix}\rho\\ \rho u\\ \rho v\\ \rho w\\ \rho e\end{bmatrix}+\frac{\partial}{\partial x}\begin{bmatrix}\rho u\\ \rho u^2+p\\ \rho uv\\ \rho uw\\ \rho u h_0\end{bmatrix}+\frac{\partial}{\partial y}\begin{bmatrix}\rho v\\ \rho uv\\ \rho v^2+p\\ \rho vw\\ \rho v h_0\end{bmatrix}$$

$$+\frac{\partial}{\partial z}\begin{bmatrix}\rho w\\ \rho uw\\ \rho vw\\ \rho w^2+p\\ \rho w h_0\end{bmatrix}=0$$

The equation of state

$$\frac{p}{\rho}=(\gamma-1)\left[e-\frac{u^2+v^2+w^2}{2}\right]$$

and the definition of total enthalpy

$$h_0=e+\frac{p}{\rho}$$

close the set of equations. Introducing the conical variables

$$\xi=\frac{y}{x},\qquad \eta=\frac{z}{x},\qquad r=\sqrt{x^2+y^2+z^2}$$

and assuming conical self-similarity (that the solution is independent of r), the Euler equations become

$$\frac{r}{\sqrt{1+\eta^2+\xi^2}}\frac{\partial}{\partial t}\begin{bmatrix}\rho\\ \rho u\\ \rho v\\ \rho w\\ \rho e\end{bmatrix}+\frac{\partial}{\partial \xi}\begin{bmatrix}\rho(v-\xi u)\\ \rho u(v-\xi u)-\xi p\\ \rho v(v-\xi u)+p\\ \rho w(v-\xi u)\\ \rho h_0(v-\xi u)\end{bmatrix}$$

$$+\frac{\partial}{\partial \eta}\begin{bmatrix}\rho(w-\eta u)\\ \rho u(w-\eta u)-\eta p\\ \rho v(w-\eta u)\\ \rho w(w-\eta u)+p\\ \rho h_0(w-\eta u)\end{bmatrix}+2\begin{bmatrix}\rho u\\ \rho u^2+p\\ \rho uv\\ \rho uw\\ \rho u h_0\end{bmatrix}=0$$

In the above, the unsteady terms have been included so that an iterative procedure may be employed to reach a conically self-similar steady state. The equations are solved on the unit sphere by setting $r=1$.

The physical boundary conditions consist of a no-flux condition at the wing, freestream conditions outside the bow shock, and a Kutta condition at the leading edge of the wing. The third condition is enforced implicitly by the truncation error and artificial viscosity of the numerical method. The implementation of the other two conditions will be discussed in the next section.

Solution Procedure

The basic solution scheme is a finite-volume spatial discretization with a multistage integration in time, as proposed by Jameson et al.[15] Local time-stepping and mesh-sequencing are used to accelerate the convergence to steady state.

The set of partial differential equations for conical flow may be written in the form

$$\frac{r}{\sqrt{1+\eta^2+\xi^2}}\frac{\partial}{\partial t}U+\frac{\partial}{\partial \eta}F+\frac{\partial}{\partial \xi}G+2H=0$$

and is discretized as

$$\frac{r}{\sqrt{1+\eta^2+\xi^2}}\frac{\mathrm{d}U_{ij}}{\mathrm{d}t}A_{ij}+\sum_{\ell=1}^{4}\left[F_\ell\Delta\eta_\ell-G_\ell\Delta\xi_\ell\right]+2H_{ij}A_{ij}=0$$

where A_{ij} is the area, and $\Delta\eta_\ell$ and $\Delta\xi_\ell$ are the projected side lengths of the four sides of a computational cell. This scheme requires added second- and fourth-difference damping to capture shocks and yield smooth solutions. The damping formulation adopted follows Rizzi and Eriksson.[16] The second-difference damping is pressure-weighted, and is of the form

$$D_2(U)=\nu_2\left[\delta_i\left(\frac{\delta_i^2 p}{\max|\delta_i^2 p|}\delta_i U\right)+\delta_j\left(\frac{\delta_j^2 p}{\max|\delta_j^2 p|}\delta_j U\right)\right]$$

where δ_i and δ_j are undivided central-difference operators defined by

$$\delta_i(U_{i,j})=U_{i+\frac{1}{2},j}-U_{i-\frac{1}{2},j},\qquad \delta_j(U_{i,j})=U_{i,j+\frac{1}{2}}-U_{i,j-\frac{1}{2}}$$

The pressure switch is normalized to take values from zero (low-pressure gradient regions) to one (high-pressure gradient regions). It was found to be necessary to set the pressure switch to one at several cells in the vicinity of the leading edge and the hinge. The second-difference damping is proportional to the mesh spacing. A damping coefficient of $\nu_2=0.05$ was used for the second-difference damping.

The fourth-difference damping is unweighted, and of the form

$$D_4(U)=\nu_4\left[\delta_i^4 U+\delta_j^4 U\right]$$

It is not turned off in the vicinity of shocks, and is everywhere proportional to the cube of the mesh spacing. A damping coefficient of $\nu_4=0.01$ was used for the fourth-difference damping.

The body boundary condition is a no-flux condition, coupled with a pressure extrapolation of the form

$$\frac{\partial p}{\partial n}=0$$

This is implemented on the body cell faces by using the cell-center pressure to evaluate the fluxes, keeping only the pressure terms in the flux balance. The error in this is directly proportional to the grid spacing and the dynamic pressure, and inversely proportional to the radius of curvature of the streamlines. The approximation is good both on the wing, where the radius of curvature is zero, and on the body, where the crossflow component of the velocity is small.

The far-field boundary condition is enforced by prescribing an outer boundary to the computational domain such that the bow shock lies entirely inside the computational domain. Freestream conditions are then enforced at the outer boundary. The bow shock is captured by the solution scheme.

The grids are generated by solving the system

$$\alpha\xi_{ii} - 2\beta\xi_{ij} + \gamma\xi_{jj} = -J^2\left[P\xi_i + Q\xi_j\right]$$

$$\alpha\eta_{ii} - 2\beta\eta_{ij} + \gamma\eta_{jj} = -J^2\left[P\eta_i + Q\eta_j\right]$$

where $\alpha = \xi_j^2 + \eta_j^2$, $\beta = \xi_i\xi_j + \eta_i\eta_j$, $\gamma = \xi_i^2 + \eta_i^2$, $J = \xi_i\eta_j - \xi_j\eta_i$, and the subscripts denote differentiation with respect to the computational coordinates. The source terms P and Q on the body and the outer boundary are calculated to enforce orthogonality and a specified cell aspect ratio. These source terms are extended into the field, decaying exponentially away from the boundaries. The method is outlined fully in Steger and Sorenson.[17] The geometry that is used for the calculations is the cross section at 90% of the configuration length. The conical self-similarity assumption implies that this section is extended conically fore and aft. A section of a typical grid is shown in Fig. 2. All calculations were carried out on a grid of 128×128 cells. In all of the plots, the ξ and η coordinates are normalized by the value of ξ at the leading edge of the uncambered wing (i.e., cot Λ).

Experimental Setup and Models

The experimental results in this paper are from a series of tests performed in the spring of 1985 at NASA Langley Research Center. The experimental setup is described fully elsewhere.[18,19]

The models consisted of a series of four delta wings, three with camber and one without, each with a leading-edge sweep of 75 deg and the same upper surface wetted area. The reference flat delta wing had a span of 18 in. and a length of 33.588 in. Wing camber was generated for the other three wings by a deflection of the outboard 30% of the local wing semispan to angles of 5, 10, and 15 deg, measured in the streamwise direction. To minimize the effect of airfoil shape and thickness, the leading edge was made sharp (10 deg angle normal to the wing leading edge located on the lower surface) and the upper surface was flat. A minimum balance housing was incorporated into the model.

The leeward surface of each model was instrumented with six semispan rows of 19 evenly spaced pressure orifices located at 10, 20, 30, 60, 80, and 90% of the model length. Pressure orifices were distributed over the semispan of all wings at equal distances measured along the model upper surface from 0 to 90% of the local semispan. Pressure data were obtained from a scanning valve pressure transducer mounted external to the wind tunnel.

The models were connected to the permanent model-actuating system of the tunnel by a six-component strain gage balance and sting arrangement. The balance was housed in a minimum body that was symmetrically integrated into the wing geometry. During the test, the angle of attack was measured with an accelerometer located in the permanent model-actuating system and was corrected for tunnel flow angularity and sting deflection. Force and moment data were corrected to freestream static pressure at the balance chamber.

The tests were conducted in the low Mach number test section of the Langley Unitary Plan Wind Tunnel, which is a variable Mach number, variable pressure, continuous-flow, supersonic tunnel. The test section is approximately 4 ft $\times$ 4 ft $\times$ 7 ft long. This facility is described in more detail by Jackson et al.[20] The nominal Reynolds number was 2×10^6/ft. To ensure fully turbulent boundary-layer flow over the model at attached flow conditions, according to the guidelines set forth by Braslow and Knox,[21] transition strips composed of #60 carborundum grit were sprinkled on the upper surface 0.2 in. behind the model leading edge (measured normal to the leading edge). The transition strips were approximately 0.0625 in. wide.

Results

The cases chosen for study in this paper are outlined in Table 1. They were chosen so as to show the effects of Mach number, angle of attack, and flap angle on the flowfield. Both nominal and actual angle-of-attack values are given in Table 1; the computations were carried out at the actual angle of attack for each case.

Case 1: $M = 1.7$, $\alpha = 4$ deg, $\delta = 5$ deg

The computational and experimental results for this case are presented in Figs. 3 and 4. Figure 3 shows the contours of total pressure loss in the computed solution. This parameter turns out to be a useful one for vortical Euler solutions, since a vortex or vortex sheet is accompanied by a corresponding total pressure loss.[12] This particular plot, therefore, implies a sheet emanating from the leading edge, reattaching approximately halfway up the flap, and separating again at the hinge line. There is a vortex that covers the outboard half of the flap, and one on the portion of the wing inboard of the hinge line. Although the vapor screen (inset in Fig. 3) barely shows evidence of either vortex, the experimentally measured surface pressures (symbols in Fig. 4) show evidence of the leading-edge separation and the reattachment on the flap. There does not seem to be evidence of a vortex over the portion of the wing inboard of the hinge line in the measured surface pressure distribution. The computed surface pressures (the solid line in Fig. 4) overpredict the suction peaks on the wing and the flap.

Case 2: $M = 1.7$, $\alpha = 4$ deg, $\delta = 10$ deg

The computational and experimental results for this case are shown in Figs. 5 and 6. The total pressure loss contours (Fig. 5) show a shear layer, generated at the leading edge. The shear layer is convected along the flap, separating at the hinge line to form a vortex that resides inboard of the hinge. This vortex is visible in the vapor screen (inset in Fig. 5). The existence of a shear layer, as opposed to a vortex, on the flap is substantiated by the lack of a suction peak in either the experimental or computed surface pressure (Fig. 6). The

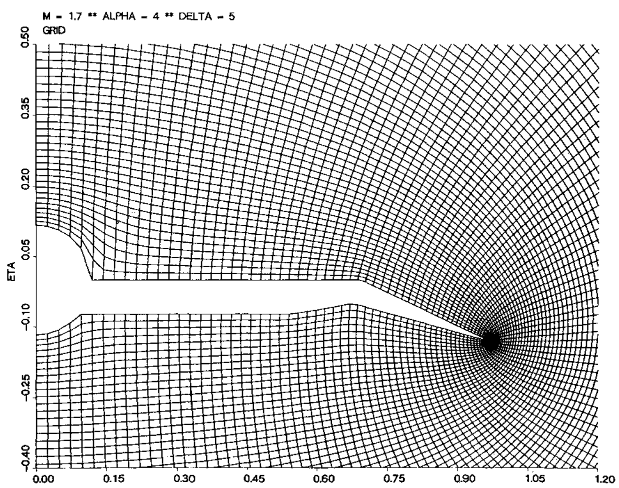

Fig. 2 Detail of typical grid.

Table 1 Test cases

Case	M	α_{nom}, deg	α_{act}, deg	δ, deg
1	1.7	4	4.30	5
2	—	—	4.20	10
3	—	8	8.84	5
4	—	—	8.68	10
5	2.4	4	3.84	10
6	—	12	12.68	10

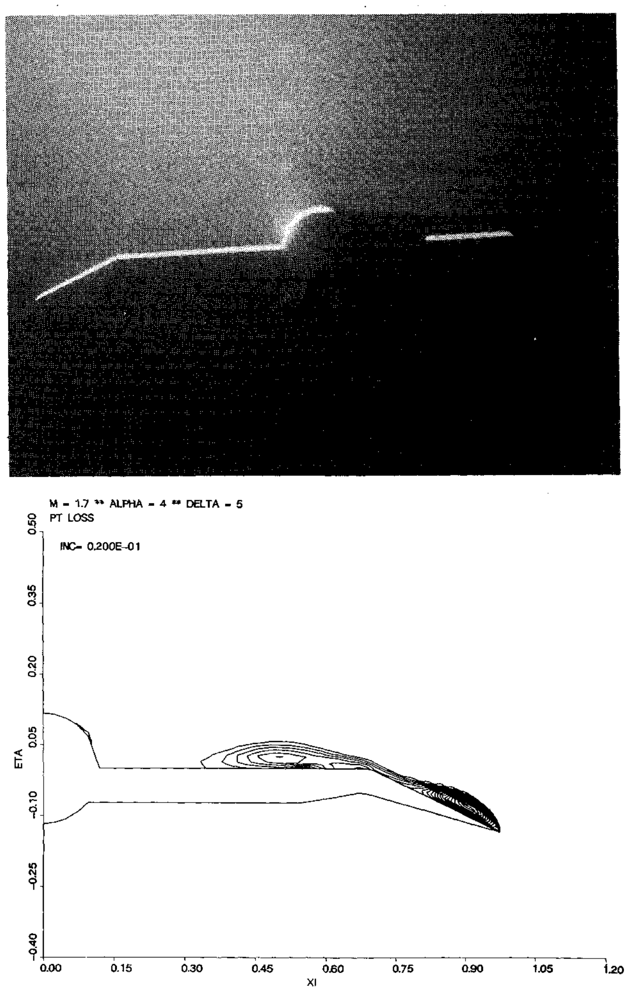

Fig. 3 Case 1: total pressure loss contours and vapor screen.

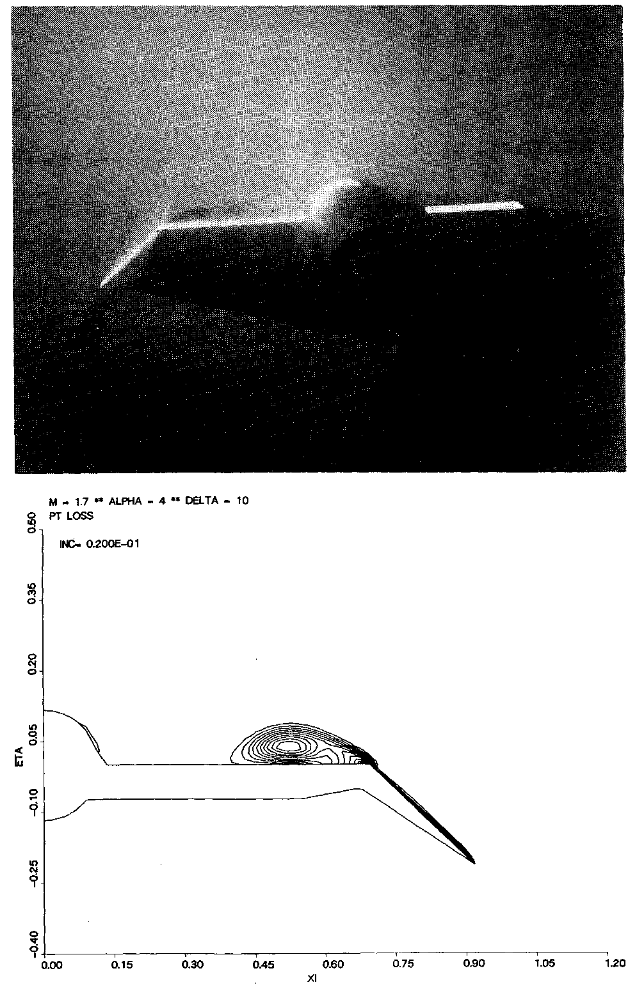

Fig. 5 Case 2: total pressure loss contours and vapor screen.

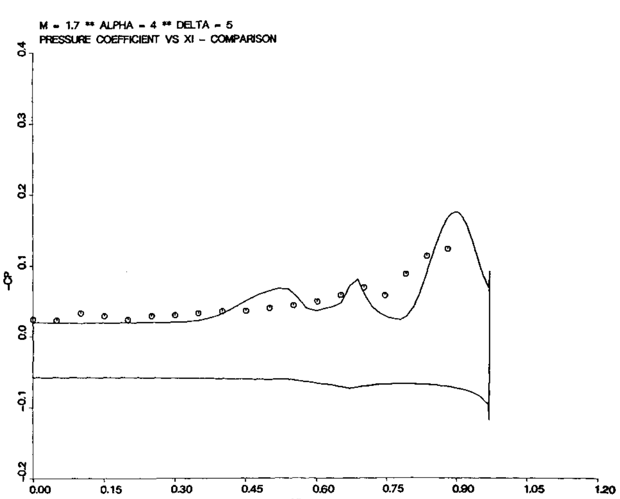

Fig. 4 Case 1: surface pressure coefficient comparison.

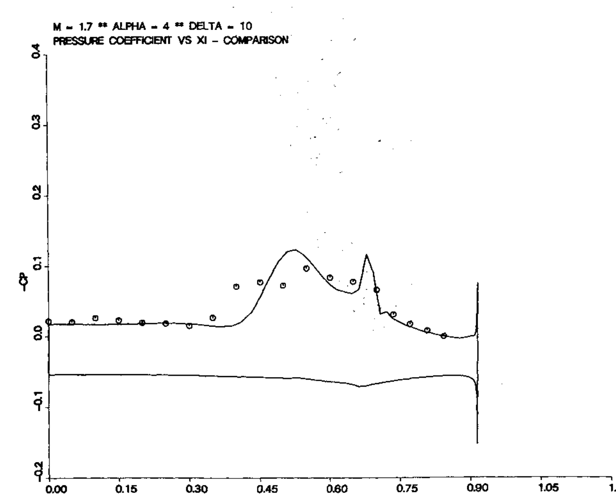

Fig. 6 Case 2: surface pressure coefficient comparison.

surface pressure coefficients compare well on the flap and at the leeward symmetry line. The computation shows a spike in the surface pressure coefficient at the hinge line that is spurious. This effect shows up to a greater or lesser extent in all of the vortex flap calculations. The experimental surface pressures (symbols) show a secondary suction peak, just inboard of the hinge, which is not predicted by the computation (solid line). The computed primary suction peak is stronger than that seen experimentally. The fact that the Euler solution predicts a primary suction peak that is farther outboard and stronger than that seen experimentally is characteristic of the inviscid model, and has been noted elsewhere.[6] It will be observed in most of the results presented here.

Case 3: $M = 1.7$, $\alpha = 8$ deg, $\delta = 5$ deg

The computational and experimental results for this case are shown in Figs. 7 and 8. The total pressure loss contours

(Fig. 7) indicate a sheet emanating from the leading edge, rolling up into a vortex that straddles the hinge line. There is also evidence of a vortex of opposite sense on the flap. The vapor screen (inset in Fig. 7) shows a large leading-edge vortex that straddles the hinge. Details on the flap cannot be made out. There is a vortex on the flap, seen in both the experimental and computed surface pressures (Fig. 8). The surface pressures in this case agree quite well, except in the immediate vicinity of the hinge. The Euler calculations predict the vortex too far outboard. This was the only case for which the computations were difficult to converge to a steady state.

Case 4: $M = 1.7$, $\alpha = 8$ deg, $\delta = 10$ deg

Figures 9 and 10 show the computational and experimental results for this case. The total pressure loss contours (Fig. 9) show two distinguishable sets of closed contours, one directly above the flap and the other immediately inboard of the hinge line. The vapor screen for this case (inset in Fig. 9) is hard to read, but suggests that the core of the vortex is farther inboard than predicted. The surface pressure coefficient comparison (Fig. 10), however, shows that the location of the two vortices is predicted correctly, but the suction peaks are overpredicted. Again, the surface pressure spike seen at the hinge line in the computations does not appear in the measurements.

Case 5: $M = 2.4$, $\alpha = 4$ deg, $\delta = 10$ deg

The computational and experimental results for this case are shown in Figs. 11–14. The total pressure loss contours show an entirely different character than those of any of the other cases. There is a set of close contours inboard of the hinge, suggesting a vortex that resides inboard of the hinge, but there is no loss generated at the leading edge. This suggests that the flow is almost exactly tangent to the leading edge. The crossflow streamlines (Fig. 12) show this to be the case. The hinge-line vortex is clear in the vapor screen (inset in Fig. 11). There is no evidence of a sheet on the flap. The crossflow velocity vectors (Fig. 13) show both the hinge-line vortex and the lack of shear on the flap. The surface pressure comparison is good on the flap and near the symmetry line (Fig. 14). The suction peak is overpredicted and placed too far outboard.

Case 6: $M = 2.4$, $\alpha = 12$ deg, $\delta = 10$ deg

Figures 15–18 present the computational and experimental results for this case. This case differs from the other in that

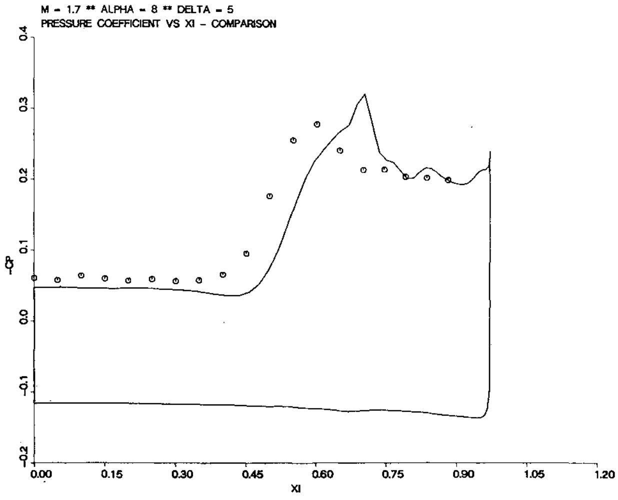

Fig. 8 Case 3: surface pressure coefficient comparison.

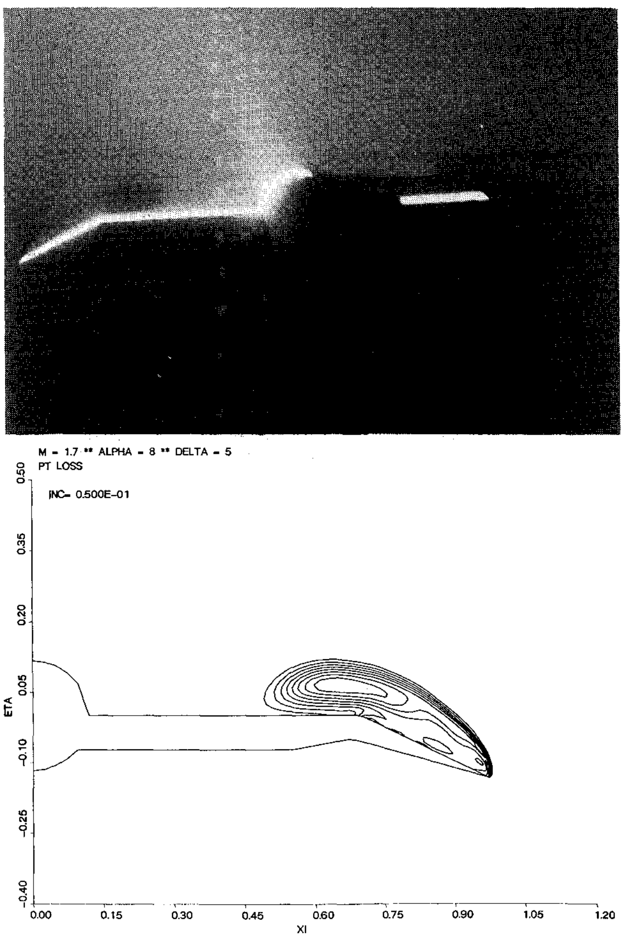

Fig. 7 Case 3: total pressure loss contours and vapor screen.

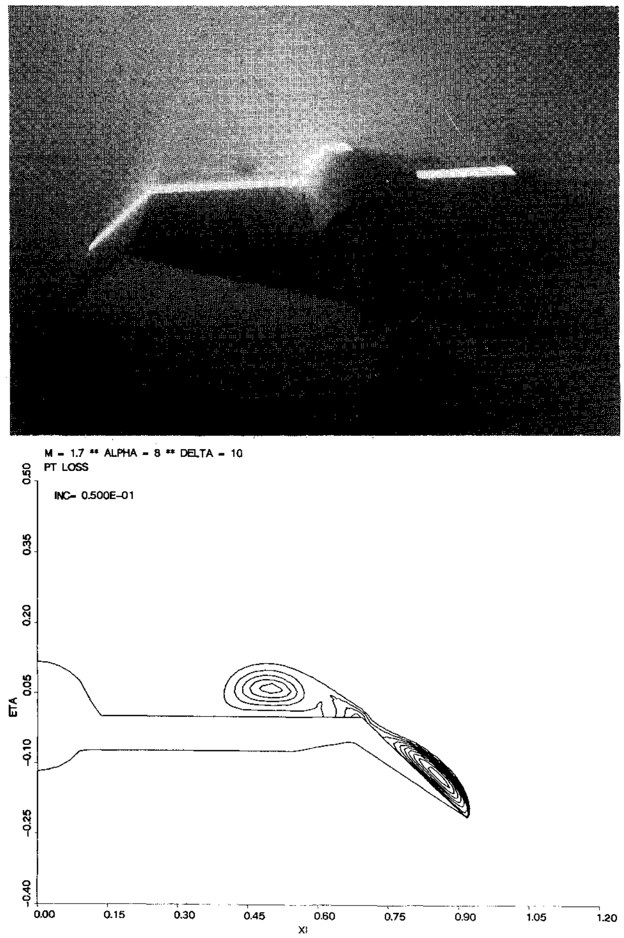

Fig. 9 Case 4: total pressure loss contours and vapor screen.

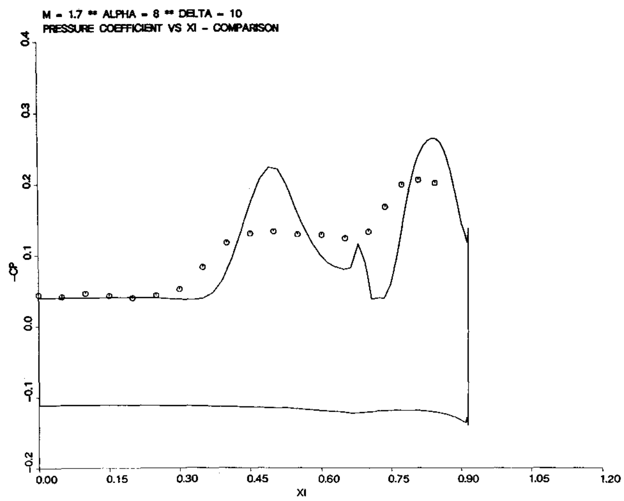

Fig. 10 Case 4: surface pressure coefficient comparison.

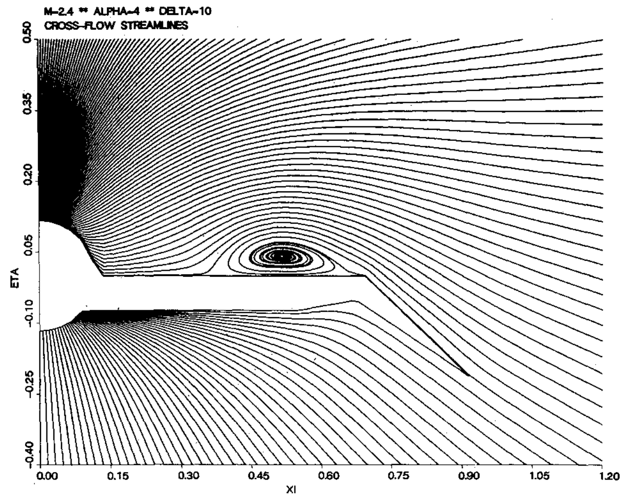

Fig. 12 Case 5: crossflow streamlines.

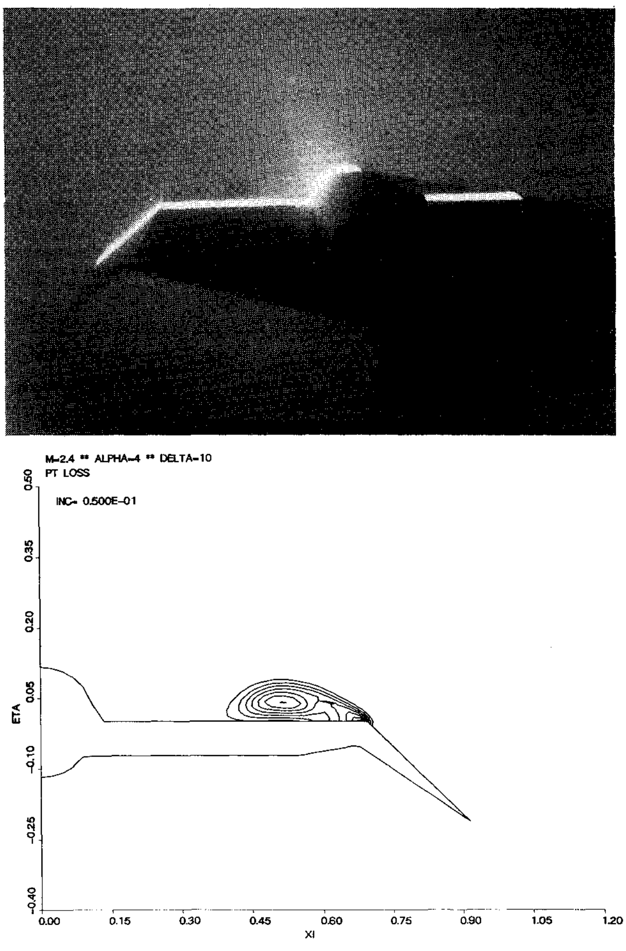

Fig. 11 Case 5: total pressure loss contours and vapor screen.

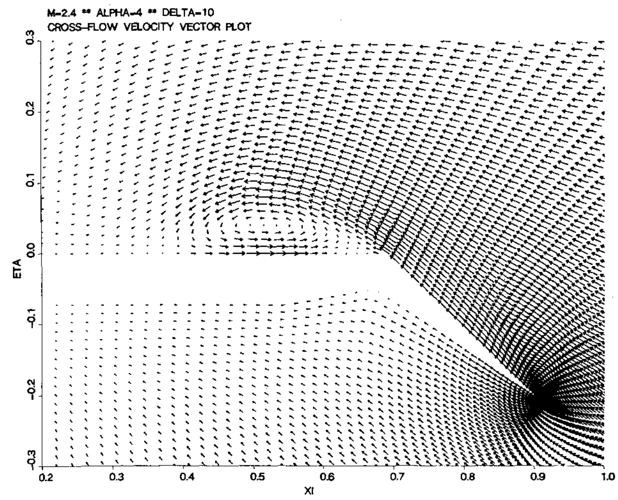

Fig. 13 Case 5: crossflow velocity vectors.

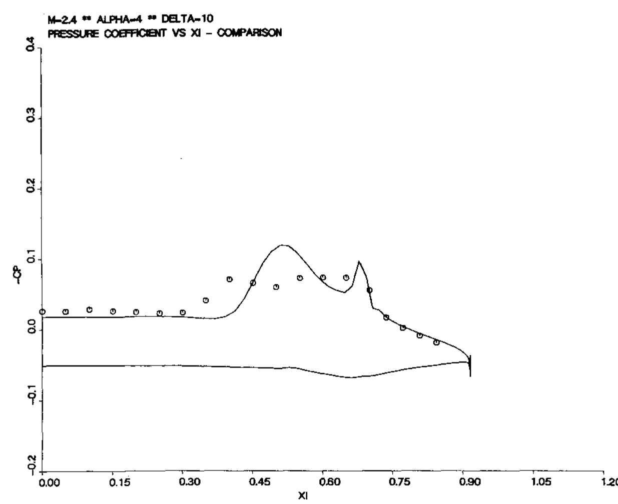

Fig. 14 Case 5: surface pressure coefficient comparison.

crossflow shocks have formed under the vortex and above the feeding sheet. There is a vortex on the flap, a primary vortex above the inboard portion of the wing, and a crossflow shock under the primary vortex. There is also evidence in the total pressure loss contours (Fig. 15) of a small vortical region just inboard of the hinge, below the sheet that feeds the primary vortex. In the vapor screen (inset in Fig. 15), the sheet and the primary vortex are visible, and there is an indication of a sheet or a vortex on the flap. The crossflow shock above the sheet feeding the vortex can be seen. The crossflow velocity vectors (Fig. 16) show the vortices and the shock clearly, and the small vortical region just inboard of the hinge. It is interesting to note that, in the computed solution, the reverse flow on the flap is really an extension of the primary vortex. The computed crossflow is supersonic above and below both vortices, and reaches a Mach number of 1.5 inboard of the crossflow

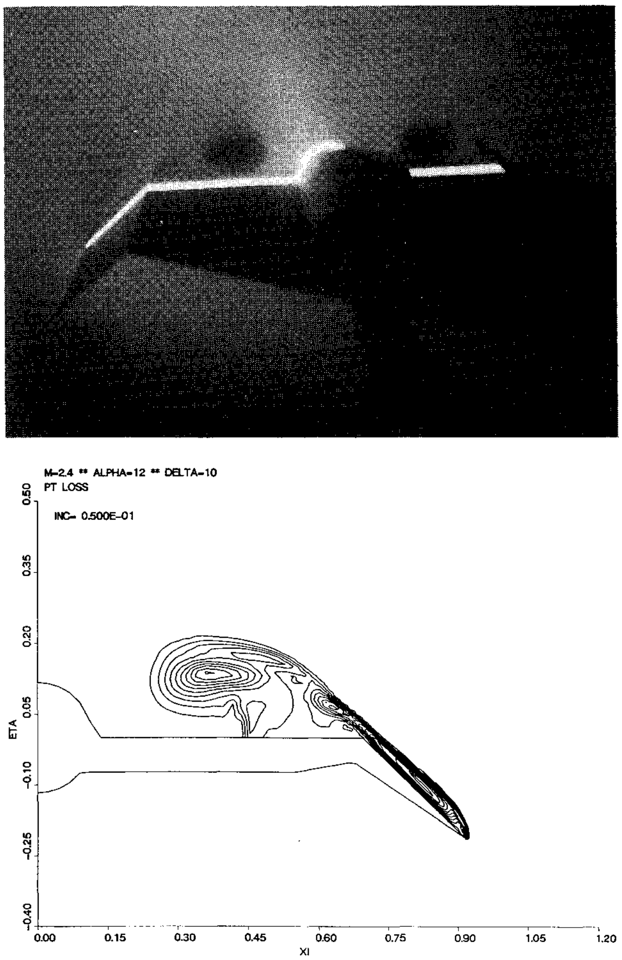

Fig. 15 Case 6: total pressure loss contours and vapor screen.

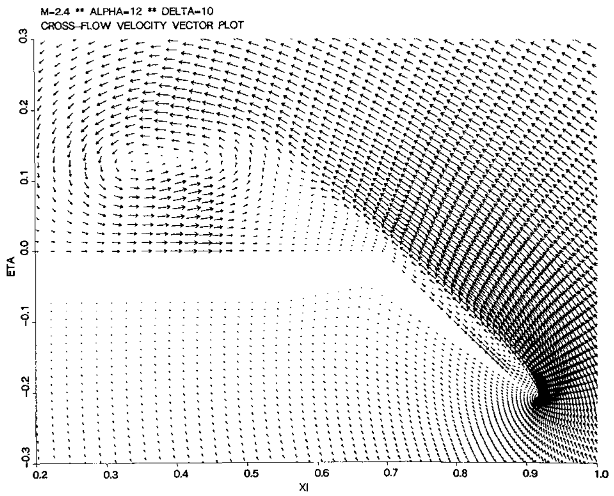

Fig. 16 Case 6: crossflow velocity vectors.

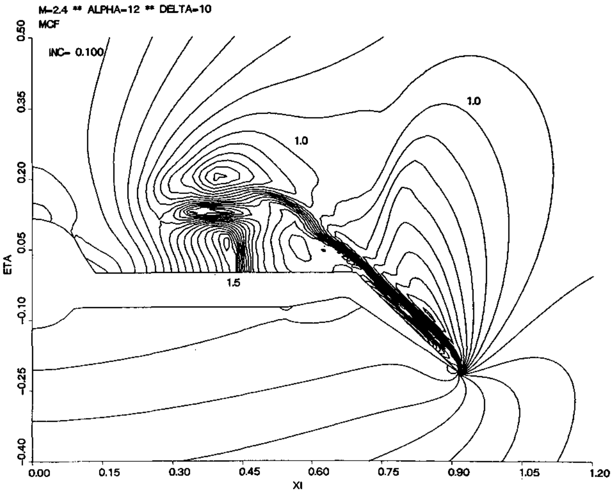

Fig. 17 Case 6: crossflow Mach number contours.

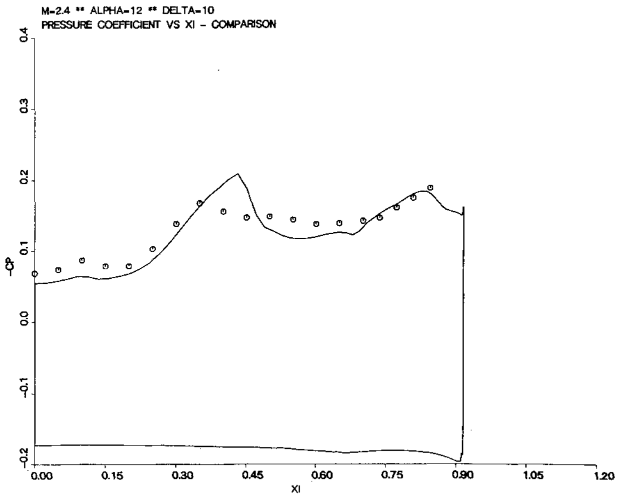

Fig. 18 Case 6: surface pressure coefficient comparison.

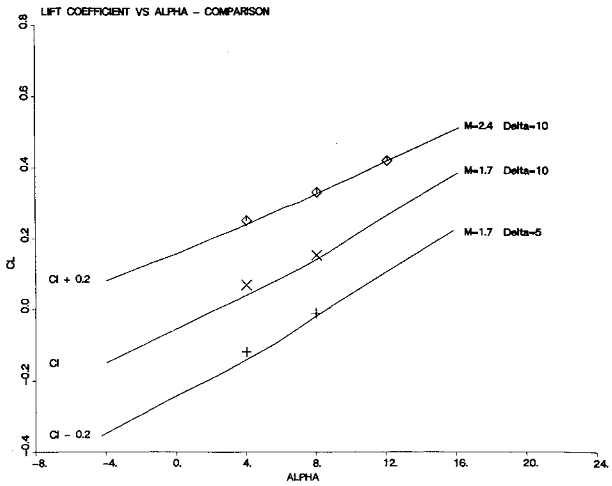

Fig. 19 C_l vs α.

shock (Fig. 17). The measured surface pressure coefficient (Fig. 18) does not show evidence of a crossflow shock. This could be due to the fact that the Euler calculations overpredict the expansion under the vortex. Elsewhere, the surface pressures agree well.

Lift Coefficient Calculation

Figure 19 is a plot of the lift coefficient as a function of α for three cases: $M = 1.7$ and $\delta = 5$ deg; $M = 2.7$ and $\delta = 10$ deg; $M = 2.4$ and $\delta = 10$ deg. The lines are the experimental data, constructed from 13 data points each. The $M = 1.7$, $\delta = 5$ deg data is offset by -0.2 on the C_l axis, and the $M = 2.4, \delta = 10$ deg data is offset by $+0.2$ on the C_l axis to keep the three lines from falling on top of each other. The symbols represent the computed lift coefficients, and are offset in the same manner as the experimental data. As can be seen, the lifts compare well, with the computations slightly overpredicting the lift at the lower angles of attack.

Conclusions and Discussion

The detailed comparison of seven cases serves to assess the strengths and weaknesses of an Euler equation model for vortex-flap studies. The strengths are that the total pressure loss contours and the crossflow velocity vectors indicate the same flow features that the vapor screens and tufts do, and the lift coefficients are in good agreement with experiment. The surface pressures agree well, but two general trends can be seen: the suction peak tends to be overpredicted, and the vortex tends to be predicted too far outboard. Although Navier-Stokes solvers are necessary to calculate moment and drag coefficients, the Euler methods, which are much less expensive computationally, show promise as a tool in understanding leading-edge vortex flows. To illustrate the low computational cost of these solutions, all of the computational and graphical analysis for this paper was done on a VAXSTATION II at the rate of about one case per day.

It is clear that a variety of flow structures are possible, and in some cases they are quite sensitive to angle of attack and flap angle. It appears that only a narrow range of these parameters will lead to a vortex being contained on the flap. The reliability of the Euler solutions in predicting whether the vortex resides on the flap, straddles the hinge, or resides inboard of the hinge indicates that the Euler solver could provide a good preliminary design tool for vortex-flap geometries. Detailed force and moment predictions would follow with a Navier-Stokes model.

The solutions were insensitive to computational parameters; grid refinement had the most effect on the solutions. The mesh refinement mostly acts to steepen up gradients in the flowfield. The suction peak is more pronounced on the finer meshes. Also, the pressure spike seen at the hinge in most of the calculations becomes more localized on the finer meshes. A look at results on a coarser mesh indicate that refinement will have little effect on the lift, less than a 1% change by refining the mesh by a factor of two in each direction.

In summary, the comparisons between the wind-tunnel data and the conical Euler solutions given in this paper show the strengths and weaknesses of the conical Euler model. The model tends to overpredict the suction, due to the primary vortex and the compression at the hinge line, but still gives a good estimate of the lift. Although it cannot model viscous effects, most notably the boundary layer and the secondary vortex, it does model the gross features of the flow quite well. Clearly, a viscous model is needed to examine the hinge line, the secondary vortex or the boundary layer, or to calculate drag or moment coefficients. Also, a three-dimensional model would be needed to study any effects at the apex or trailing edge of the wing, or any of the effects, because the wing is not truly conical. The conical Euler model is also limited in that it cannot be used to study flow instabilities or other unsteady effects. However, the conical Euler solutions can be a powerful tool in studying the physics of these flows.

Acknowledgments

The computational portion of this research was supported by NASA Langley Research Center under NASA Grant NAG-1-358, monitored by Dr. Manny Salas and Mr. Duane Melson. Hardware grants were provided by the Digital Equipment Company and the United Technologies College Relations Board.

References

[1]Stanbrook, A. and Squire, L.C., "Possible Types of Flow at Swept Leading Edges," *Aeronautical Quarterly*, Vol. 15, Feb. 1964, pp. 72–82.

[2]Miller, D.S. and Wood, R.M., "Leeside Flows over Delta Wings at Supersonic Speeds," *Journal of Aircraft*, Vol. 21, Sept. 1984, pp. 680–686.

[3]Vorropoulos, G. and Wendt, J.J., "Laser Velocimetry Study of Compressibility Effects on the Flow Field of a Delta Wing," AGARD-CP-342 Paper 9, April 1983.

[4]Arlinger, B.G., "Computation of Supersonic Flow Including Leading-Edge Vortex Flows Using Marching Euler Technique," International Symposium on Computational Fluid Dynamics, Tokyo, Sept. 1985.

[5]Murman, E., Rizzi, A., and Powell, K., "High-Resolution Solutions of the Euler Equations for Vortex Flows," *Progress and Supercomputing in Computational Fluid Dynamics*, Birkhauser, Boston, MA, 1985, pp. 93–113.

[6]Murman, E.M., Powell, K.G., Miller, D.S., and Wood, R.M., "Comparison of Computations and Experimental Data for Leading-Edge Vortices—Effects of Yaw and Vortex Flaps," AIAA Paper 86-0439, Jan. 1986.

[7]Newsome, R. and Thomas, J., "Computation of Leading-Edge Vortex Flows," NASA Langley Vortex Flow Aerodynamics Conf., Hampton, VA, Oct. 1985.

[8]Rizzi, A. and Eriksson, L.E., "Computation of Inviscid Incompressible Flow with Rotation," *Journal of Fluid Mechanics*, Vol. 153, April 1985, pp. 275–312.

[9]Buter, T.A. and Rizetta, D.P., "Steady Supersonic Navier-Stokes Solutions of a 75 Degree Delta Wing at Angle of Attack," NASA Langley Vortex Flow Aerodynamics Conf., Hampton, VA, Oct. 1985.

[10]Fujii, K. and Kutler, P., "Numerical Simulation of the Viscous Flow Fields over Three-Dimensional Complicated Geometries," AIAA Paper 84-1550, June 1984.

[11]Rizetta, D.P. and Shang, J.S., "Numerical Simulation of Leading-Edge Vortex Flows," AIAA Paper 85-1544, June 1984.

[12]Powell, K., Murman, E., Perez, E., and Baron, J., "Total Pressure Loss in Vortical Solutions of the Conical Euler Equations," AIAA Paper 85-1701, July 1985.

[13]Rao, D.M., "Leading-Edge Vortex Flap Experiments on a 74-Degree Delta Wing," NASA CR-159161, 1979.

[14]Lamar, J.E. and Campbell, J.F., "Recent Studies at NASA Langley of Vortical Flows Interacting with Neiboring Surfaces," AGARD-CP-342, Paper 10, April 1983.

[15]Jameson, A., Schmidt, W., and Turkel, E., "Numerical Solutions of the Euler Equations by a Finite Volume Method Using Runge-Kutta Time-Stepping Schemes," AIAA Paper 81-1259, June 1981.

[16]Rizzi, A., and Eriksson, L.E., "Computation of Flow around Wings Based on the Euler Equations," *Journal of Fluid Mechanics*, Vol. 148, Nov. 1984.

[17]Steger, J.L. and Sorenson, R.L., "Automatic Mesh-Point Clustering Near a Boundary in Grid Generation with Elliptic Partial Differential Equations," *Journal of Computational Physics*, Vol. 33, Dec. 1979, pp. 405–410.

[18]Miller, D.S. and Wood, R.M., "An Investigation of Wing Leading-Edge Vortics at Supersonic Speeds," AIAA Paper 83-1816, July 1983.

[19]Miller, D.S. and Wood, R.M., "Lee-Side Flow Over Delta Wings at Supersonic Speeds," NASA TP-2430, June 1985.

[20]Jackson, C.M., Jr., Corlett, W.A., and Monta, W.J., "Description and Calibration of the Langley Unitary Wind Tunnel," NASA TP-1905, 1981.

[21]Braslow, A.L., and Knox, E.C., "Simplified Method for Determination of Critical Height of Distributed Roughness Particles for Boundary-Layer Transition at Mach Numbers from 0 to 5," NACA TN-4363, 1958.